

Nanoscale Schottky barrier visualization utilizing computational modeling and ballistic electron emission microscopy

Westly Nolting,^{a)} Chris Durcan, Steven Gassner, Joshua Goldberg, Robert Balsano, and Vincent P. LaBella^{b)}

Colleges of Nanoscale Science and Engineering, SUNY Polytechnic Institute, Albany, New York 12203, USA

(Received 16 March 2018; accepted 1 June 2018; published online 25 June 2018)

The electrostatic barrier at a metal semiconductor interface is visualized using nanoscale spatial and meV energetic resolution. A combination of Schottky barrier mapping with ballistic electron emission microscopy and computational modeling enables extraction of the barrier heights, the hot electron scattering, and the presence of localized charges at the interface from the histograms of the spectra thresholds. Several metal semiconductor interfaces are investigated including W/Si(001) using two different deposition techniques, Cr/Si(001), and mixed Au-Ag/Si(001). The findings demonstrate the ability to detect the effects of partial silicide formation in the W and Cr samples and the presence of two barrier heights in intermixed Au/Ag films upon the electrostatic barrier of a buried interface with nanoscale resolution. This has potential to transform the fundamental understanding of the relationship between electrostatic uniformity and interface structure for technologically important metal semiconductor interfaces. *Published by AIP Publishing.*

<https://doi.org/10.1063/1.5029913>

I. INTRODUCTION

Metal/semiconductor junctions were the first rectifying electronic devices, and today they are found in discrete diodes and nanoscale source/drain contacts in state-of-the-art finFETs.^{1–6} The electrostatic barrier that forms arises from charge transfer from the semiconductor into the metal and is also dependent upon defects and interface stoichiometry.^{7–9} The understanding and optimization of the materials, interfaces, and resulting barrier are crucial for further scaling of electronic devices at the nanoscale.

Ballistic electron emission microscopy (BEEM) is a scanning tunneling microscopy (STM) technique that provides direct measurement of the electrostatics of metal/semiconductor junctions by measuring the electrostatic barrier at the metal-semiconductor (MS) interface to nanometer length and meV energetic resolution due to the nano-positioning capability of the STM tip.^{10–13} In BEEM, a voltage is applied between the STM tip and metal which allows electrons to tunnel through vacuum into the metal. Electrons with enough energy associated with the forward momentum to exceed the Schottky barrier are collected on the backside of the semiconductor as BEEM current with an ohmic contact. Imaging with BEEM is similar to STM where the BEEM current is measured at a constant bias as a function of tip position.^{14,15} Ballistic electron emission spectroscopy (BEES) is performed by measuring the BEEM current as a function of tip bias at a fixed tip position and when fit to the Bell-Kaiser model allows extraction of the barrier height.^{16,17} Typically, numerous spectra are collected from random tip locations and averaged together to reduce noise, providing an aggregate measure of the barrier height.¹⁸ BEEM is a highly accurate measure (~ 20 meV) of Schottky barrier height owing to

its ability to measure the unbiased state of the junction.¹⁹ Numerous investigations utilizing BEEM imaging and spectroscopy to study metal-semiconductor (MS), metal-insulator-semiconductor (MIS), and novel nanoscale materials have been performed, demonstrating the unique insight of the technique.^{20–26}

Visualizing the electrostatic barrier to nanoscale dimensions is a relatively recent BEEM advancement and is accomplished by mapping the barrier height using BEES.^{12,13,27–34} Tens of thousands of spectra are collected on a regularly spaced grid and then individually fit to acquire a map of the local barrier height as well as a histogram of the spectra thresholds. The histograms of spectra thresholds contain information about the elastic scattering of the hot electrons and the interface stoichiometry.^{12,13,34} This was accomplished with the aid of simplified Monte Carlo modeling on both W/Si and Cr/Si Schottky diodes. However, this early modeling neglected inelastic hot-electron scattering and scattering from ionized impurities in the near interface region. In addition, χ^2 statistics were not utilized to find the best fit by performing exhaustive searches over the possible parameter space.

In this article, a computational model of the hot electron transport phenomenon is developed and applied to several Schottky barrier height distributions measured with ballistic electron emission microscopy on a variety of metal-semiconductor systems. The model finds the best agreement from χ^2 minimization by performing large searches over parameter spaces as specified by the user. It captures the number of barrier heights at the interface, the elastic and inelastic hot electron scattering in the metal, and the presence of isolated charges near the interface. When combined with Schottky barrier maps and histograms, this model enables discovery of the complex relationship between structural and electrostatic uniformity of a buried material interface with nanoscale resolution, and is given the name ‘Schottky barrier visualization.’

^{a)}Electronic address: wnolting@sunypoly.edu

^{b)}Electronic address: vlabella@sunypoly.edu

II. EXPERIMENTAL

The fabrication of the Schottky diodes was performed with either ultrahigh vacuum (UHV) thermal evaporation or sputter deposition on high-resistive HF-treated Si(001) single crystal substrates. Further details have been previously published.^{12,13,34} A modified low temperature UHV STM (Omicron) was used for all BEEM measurements with a base pressure in the 10^{-11} mbar range.³⁵ In this BEEM configuration, an ohmic contact to the semiconductor and a top grounding contact to the metal are made to separately measure BEEM current and STM current, respectively. The ohmic contact connects to a second pre-amplifier to measure the ballistic current. Thousands of BEEM spectra were acquired on a regularly spaced grid of tip locations over a square micron and then fit to a simplified BEEM model $I_B = A(V_t - \phi_b)^n$, where V_t is the tip bias, n is a model exponent, A is the amplitude, and ϕ_b is the Schottky barrier height. In addition, an average of all the BEEM spectra for each sample was computed. Fits were performed by linearizing the ballistic electron emission microscopy (BEEM) spectra and using a standard linear regression, which returns ϕ_b , A , and a corresponding R^2 value, indicating the quality of fit. Best fits were selected over a 0.2 eV window with a maximum R^2 value, where R^2 values less than 0.6 were considered unable to be fit.¹⁸ The exponent $n=2$ was chosen for the Au/Ag samples and $n=5/2$ for the W and Cr samples, which was based on the best agreement of the sum of the n -type and p -type Schottky barriers to the bandgap of silicon for each metal.^{12,13,18,34}

III. MODELLING

Computational modeling of the hot-electron and interface physics provides physical insight into the histograms of the BEEM spectra thresholds. The modeling computes histograms of voltage thresholds by simulating the transmission of the hot electrons through the metal and interface. The best fit between the modeled and measured histogram is determined by searching over billions of possible combinations of input parameters, while minimizing $\chi^2 = (\sum_i^N (x_i - y_i)^2 / y_i) / (N - D)$, where x_i is the data, y_i is the model, N is the number of bins, and D is the number of parameters in the model. The search range and resolution for each input parameter are specified *a priori*.

The physical effects in the model are broadly split into two categories: those arising from the interface and those arising from the hot-electron transport. The interface is modeled by specifying a Schottky barrier height ϕ_b along with a standard deviation σ . Multiple barrier heights can be specified with a mixture ratio R_ϕ to model the relative presence of each barrier at the interface. This captures any nonuniformities in the electrostatic potential that may arise due to structural or chemical disorder such as silicide formation or the presence of multiple metal species. Coulomb scattering from ionized impurity atoms in the near interface region of the semiconductor is captured by specifying the sign, magnitude, and number of the charges with a randomized position relative to the interface. This captures the local adjustments to the electrostatic potential from dopant atoms, or unintended charged foreign species introduced into the semiconductor

during sample fabrication, which appear as thresholds above or below the mean barrier height for negative or positive charged impurities, respectively. The temperature, binding energy, and dopant density are specified to model Debye length screening and ionization probability. The aggregate charge per unit depth from the interface in units of e/nm is recorded to capture this effect.

The hot electron transport and scattering phenomena in the metal are captured by a kinetic Monte Carlo (KMC) approach using independent elastic and inelastic scattering parameters Γ_e and Γ_i , respectively. Γ_e is the probability of an electron to elastically scatter, which randomly redirects the momentum vector away from the normal to the interface. This captures any momentum scattering that may arise from defects, grain boundaries, or other sources. When $\Gamma_e = 0\%$ the distributions are symmetric and become skewed to higher energies as Γ_e increases as displayed in Fig. 1. Γ_i is computed from the thickness of the metal, t , and the energy of the electron E using: $\Gamma_i(t, E) = 1 - \exp[-t/\lambda_i(E)]$, where $\lambda_i(E)$ is the inelastic mean free path. Fermi liquid theory is utilized to model inelastic mean free path: $\lambda_i(E) = \sqrt{2m_e E} / [a_0(E - E_F)^2]$, where m_e is the electron mass, E_F is the Fermi energy of the metal, and a_0 is a metal-dependent parameter obtained from theory (e.g., $a_0^{Ag} \approx 5.0 \times 10^{13} \text{ s}^{-1} \text{ eV}^{-2}$).³⁶ Inelastic events reduce the total energy of the electron and greatly reduces the probability that electrons with high energies overcome the barrier and appear in the histogram as displayed in Fig. 1.

The simulations perform probabilistic elastic and inelastic scattering calculations for each electron at every energy and use the resulting momentum normal to the interface to determine if the electron is able to overcome the barrier. If successful, the electron's initial energy is recorded in the

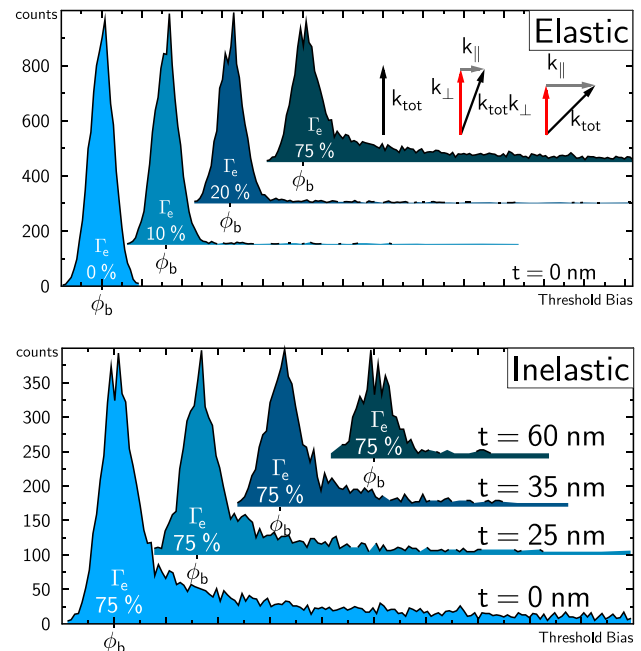


FIG. 1. Computational modeling results and the effect of elastic and inelastic scattering. The elastic modeling shows a high energy tail appearing as the elastic scattering probability is increased while the inelastic modeling shows only an overall decrease in counts in each bin.

histogram as the local barrier height. An algorithmic description of the model is described in [Appendix A](#).

IV. RESULTS

To illustrate the agreement between the modeling and the data, a histogram of the simulated thresholds is plotted in one color over the measured thresholds in another color which results in a region of agreement in a different color. The histograms and maps of the BEEM spectra thresholds for the tungsten samples fabricated with e-beam and sputter deposition are displayed in Fig. 2.¹² The map of the electron beam deposited tungsten is disordered and the histogram is broad with mean threshold and standard deviation of

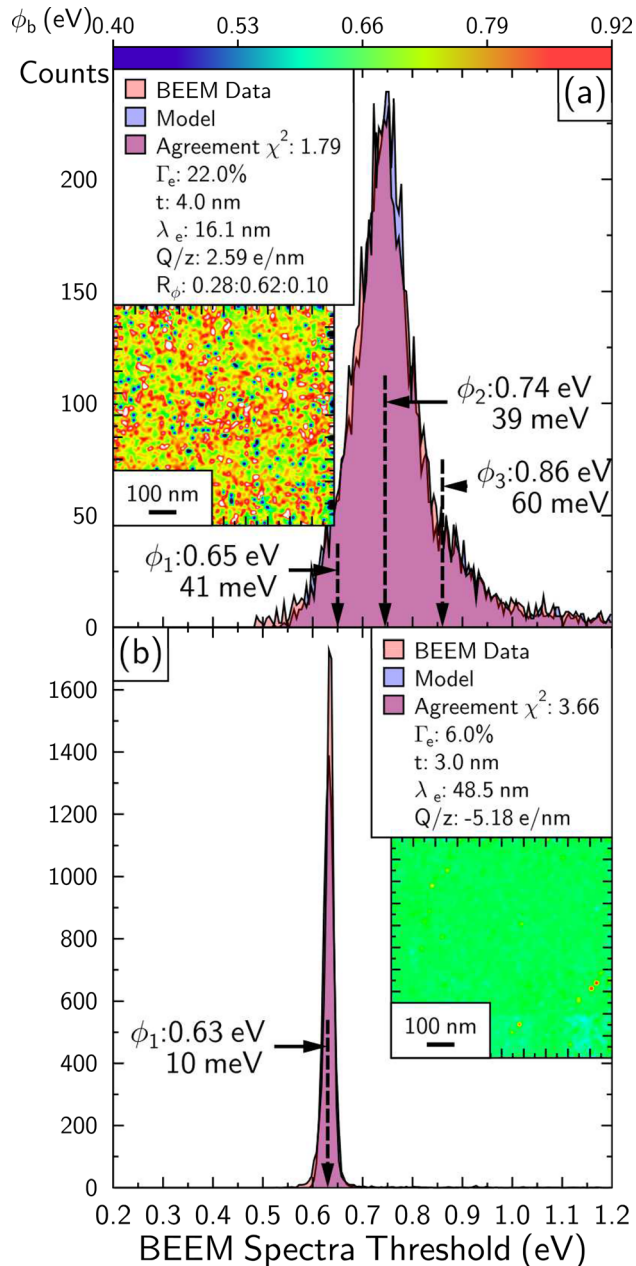


FIG. 2. The tungsten-silicon Schottky maps (inset), spectra threshold distributions, and results from modeling for (a) e-beam deposited W and (b) sputter deposited tungsten are shown indicating the barrier heights and standard deviations for the each model.

$\bar{\phi}_t = 0.76 \text{ eV}$ and $\sigma = 102 \text{ meV}$, respectively. A model with three barrier heights with the indicated ratios R_ϕ provided the best fit to the data for electron beam deposited tungsten with $\chi^2 = 1.79$, $\Gamma_e = 22\%$, $t = 4.0 \text{ nm}$, including an aggregate interface charge of 2.59 e/nm . The map of the sputter deposited tungsten is more uniform and the histogram is narrow with mean threshold and standard deviation of $\bar{\phi}_t = 0.63 \text{ eV}$ and $\sigma = 10 \text{ meV}$, respectively. A model with a single barrier height fits the sputtered sample the best with $\chi^2 = 3.66$, $\Gamma_e = 6.0\%$, $t = 3.0 \text{ nm}$ and an aggregate interface charge of -5.18 e/nm .

To demonstrate the improvement in the agreement between the data with an increasing number of parameters, several simulations are fit to the e-beam tungsten data and displayed in Figs. 3(a)–3(f). A fit to a model with a single fixed barrier height equal to the mean of the data and a single adjustable elastic scattering parameter is displayed in Fig. 3(a).¹² This model has a high χ^2 value but captures the skewing to high energies. A model with fully adjustable parameters and only a single barrier height is displayed in Fig. 3(b) and with interface charge in Fig. 3(c). A model with two barrier heights without and with interface charge is displayed in Figs. 3(d) and 3(e), respectively. A model with three barrier heights without interface charge is displayed in Fig. 3(f). A log plot of the corresponding χ^2 parameter for all the models in the figure including the best fit histogram found in Fig. 2(a) is displayed in Fig. 3(g). This plot shows a systematic decrease in χ^2 as parameters are added to the model. A plot of the corresponding elastic and inelastic scattering parameters for all the models in the figure including the best fit histogram found in Fig. 2(a) is displayed in Fig. 2(h). This plot shows an overall decrease and stabilization of both values as parameters are added to the model. An accurate model is determined by a confidence level above 3σ (P-value $> 99.7\%$) and is shown in Fig. 4.⁴⁹

The histograms and maps of the BEEM spectra thresholds for two Au/Ag/Si(001) samples with 30 nm and 5 nm of Ag are displayed in Figs. 5(a) and 5(b), respectively.³⁴ The 30 nm Ag film has a nonuniform map and mean threshold of 0.76 eV and the 5 nm silver map is has similar nonuniformity with a higher mean shifted to 0.86 eV and a secondary peak or shoulder around 0.7 eV . Both histograms resulted in best fits to models with two barrier heights as indicated.

The modeling results and histograms of the BEEM spectra thresholds for Cr/Si(001) *n*-type and *p*-type samples are displayed in Figs. 6(a) and 6(b), respectively.¹³ The best fit for both samples was achieved by a model with two barrier heights as indicated, where the *p*-type sample had significantly more skewing.

V. DISCUSSION

The dramatic difference between the e-beam and sputter deposited W/Si samples arises from unintentional radiative heating of the sample during e-beam deposition, which does not occur during sputter deposition.¹² The heating promotes silicide formation which has been shown to shift the tungsten-silicon barrier height by roughly 70 meV .^{37,38} This is captured in the computational modeling which indicates

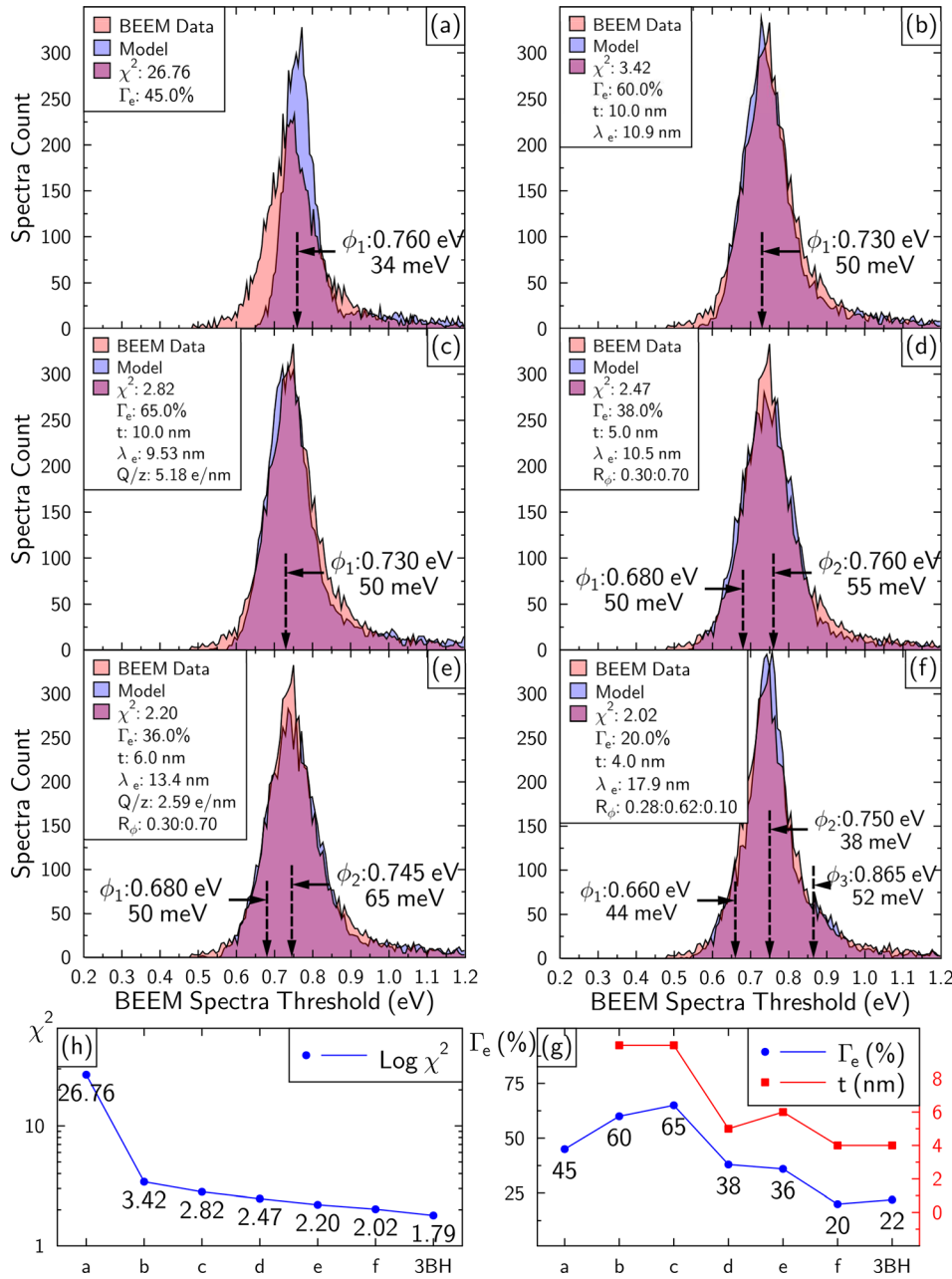


FIG. 3. (a)–(f) The effects of model parameters and number of barrier heights on the agreement to the e-beam deposited W data. (h) and (g) The progression of χ^2 and scattering rates as parameters are added.

that only one barrier height is needed for the sputter sample, whereas *three* are needed to describe the e-beam sample. The lowest barrier height ϕ_1 is attributed to W/Si(001) with a 28% contribution, where $\phi_1^{\text{sputter}} \approx \phi_1^{\text{e-beam}}$. The middle barrier height ϕ_2 is about 90 meV higher and attributed to $\text{WSi}_2/\text{Si}(001)$ and is the strongest contributor to the histogram at 62%. The highest barrier height, ϕ_3 , is in good agreement with the Au/Si(001) barrier height and attributed to gold with only a small 10% contribution.¹⁸ Prior published TEM and EDX profiling of a 10 nm wide cross section of the e-beam sample shows a significantly intermixed tungsten-silicon region when compared to the sputter sample, which showed an abrupt tungsten to silicon transition.^{12,32} The presence of a small amount of gold in the model suggests that either gold is in contact with the silicon or that a sub-nm-thick tungsten layer might not be able to “screen” the gold from affecting the barrier height in some regions. Grain

boundaries or pin-holes in the tungsten film that formed during the deposition and subsequent heating may offer potential sites for the gold to contact the silicon.

An exhaustive search over seven different simulation runs with barrier heights from one to three, with and without Coulomb scattering, was utilized to arrive at the best-fit three barrier height model for the e-beam tungsten data as summarized in Fig. 3. Previous published results of a simplified model with a fixed barrier height distribution and a single adjustable elastic scattering parameter are displayed in Fig. 3(a). This resulted in a high χ^2 but demonstrated that the skewing was caused by the elastic scattering and was the catalyst for developing the more detailed model. One of the biggest impacts in the goodness of fit is the elastic and inelastic scattering during the hot-electron transport through the metal layer. Sources of elastic scattering are grain boundaries, material interfaces, defects, and impurities.¹⁶ Elastic

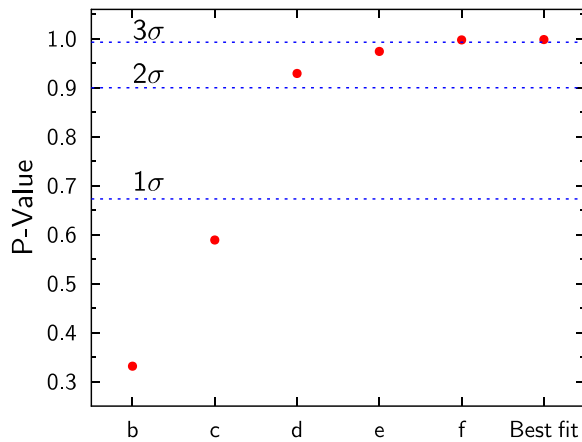


FIG. 4. Tungsten-Si computational modeling confidence levels from P-value tests using the incomplete gamma function. Best fits are obtained when modeling reaches a 3σ value for P-value tests. x-axis values correspond to modeling shown in Fig. 3.

scattering changes the perpendicular momentum of the electron relative to the metal/semiconductor interface causing the electron to need a higher energy to overcome the barrier, which skews the threshold distributions. Inelastic scattering is primarily electron-electron which dominates at energies above the barrier height and is modeled using Fermi liquid theory as previously described.

When only one barrier height is utilized, large elastic and inelastic scattering rates are needed to broaden and skew the histogram to higher energies. The histogram is also broadened by adding additional barrier heights with different energies and widths. The addition of Coulomb scattering improves the fits as well, as captured by the effective charge per unit depth. This is a small effect that allows electrons to surmount the barrier outside of the specified Gaussian distributions at lower or higher energies for positive and negative impurities, respectively. Physical sources of this effect may be ionized impurity atoms in the silicon near the interface or fluctuations in the charge density due to variations in the bonding and defects at the interface.³⁹ The lowering of χ^2 as parameters are added to the model supports their inclusion in the description of the data by increasing the confidence level above 3σ as shown in Fig. 4. The additional barriers also reduce and stabilize Γ_e and t . Multiple barrier heights resulting from incomplete silicide formation and gold interacting with silicon is a more plausible reason for the broad distribution of the e-beam sample histogram than high elastic and inelastic scattering rates. It should also be noted that both model fits of 3-barrier height with and without Coulomb scattering were above the 3σ confidence level. This indicates that while Coulomb scattering does lower the χ^2 value, both models are considered acceptable. Further description of the confidence levels are summarized in Appendix B.

The modeling of the Au/Ag/Si(001) measurements also provides insight into the structural composition of the interface as displayed in Fig. 5.³⁴ Au and Ag are miscible and intermixing of the two metals at the interface would allow both barrier heights to be measured (Ag/Si: 0.67 eV and Au/Si: 0.85 eV).¹⁸ The best fit was found with two barrier

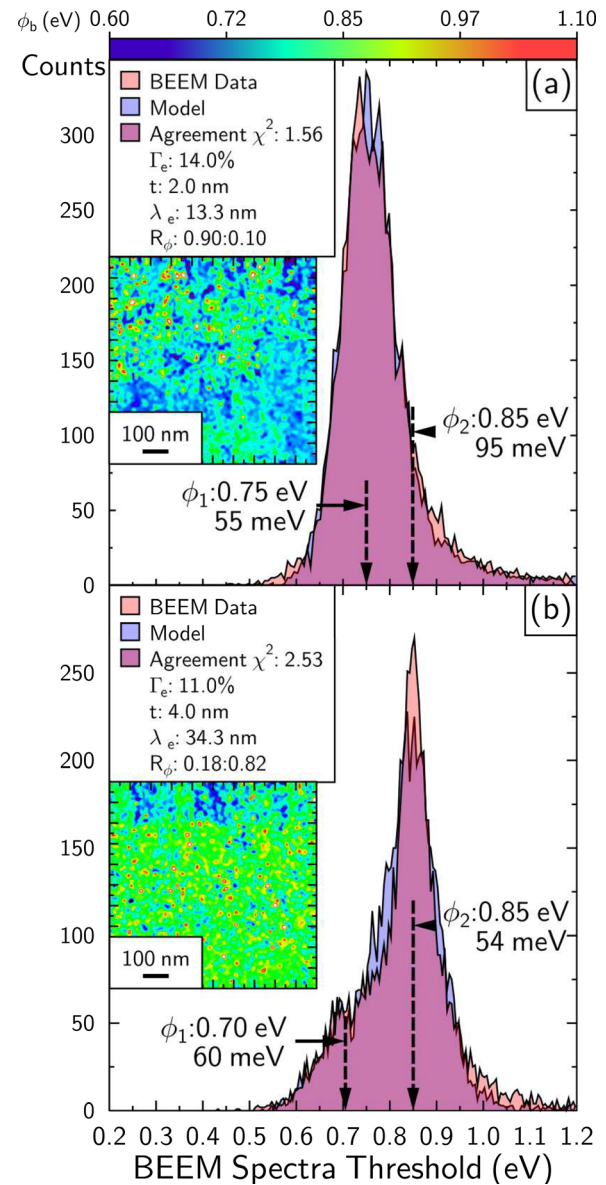


FIG. 5. Intermixed Au-Ag on n-silicon indicates detection of multiple barriers present at the interface. (a) Schottky histogram and map (inset) of (6.5 nm) Au/(30 nm) Ag indicating the two threshold values and standard deviations from the model. (b) (10 nm) Au/(10 nm) Ag indicating the two threshold values and standard deviations from the model.

heights, where the addition of Coulomb scattering did not significantly improve the fit. For both distributions of the thick (a) and thin (b) Au/Ag samples, $\phi_2 \approx 0.85$ eV corresponds to a Au/Si and the lower ϕ_1 to Ag/Si. The barrier height ϕ_1 found in the model is slightly higher than pure Ag/Si and may result from alloying or pinch off effects. It has been determined that the Schottky barrier height of AgAu alloy varies linearly with alloy composition between the Ag/Si and Au/Si barrier heights.⁴⁰ Pinch off effects occur when a nanoscale size region of one metal is surrounded by another of different barrier height.^{7,31} The included region's barrier height is altered due to the continuity of the electrostatic potential at the interface. In the 5 nm thick Ag sample, the barrier height of a nanoscale size island of silver would be increased when it is surrounded by a large volume of gold.^{18,34,41,42} The modeling predicts a Ag:Au barrier height

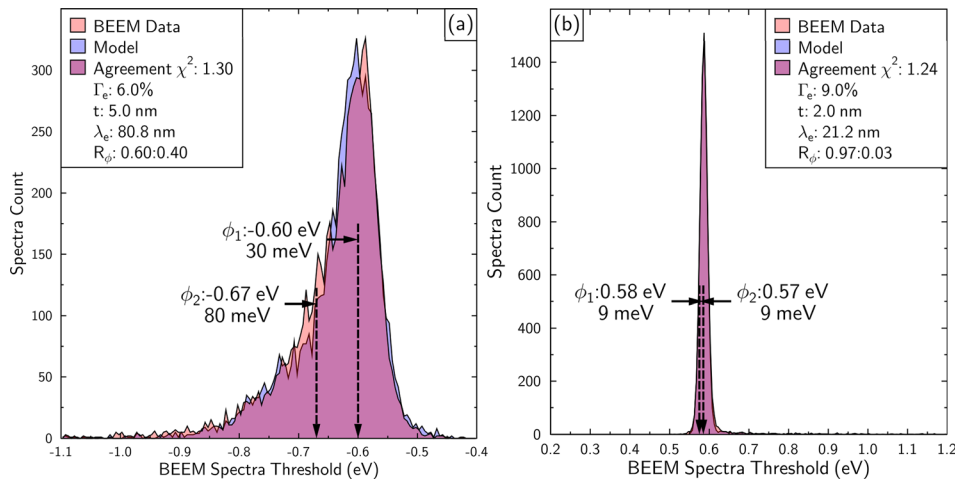


FIG. 6. Cr on n- and p-silicon with modeling efforts included. (a) Schottky histogram and modeling results of Cr/Si(001) *p*-type indicating the presence of two barriers and (b) Cr/Si(001) *n*-type indicating the presence of two barriers.

ratio of 90:10 for the 30 nm thick silver and 18:82 for the 5 nm silver. The amount of silver at the interface scales with silver thickness and these ratios are consistent with results from Auger depth profiling.³⁴

Simulations for the Cr/Si samples displayed in Fig. 6 indicated the presence of two barrier heights and attributed to silicide formation. In addition, neither Cr sample shows the presence of any gold barrier heights from the capping layer as in the W sample. These simulations are modest improvements over the previously published findings using a more simplified model that did not include inelastic scattering, interface charges, and χ^2 statistics.¹³ The Cr/Si interface and Cr-silicide formation has been shown to be complex and highly dependent upon the thickness of the chromium and may be the reason for the differences between the two samples.⁴³

The elastic and inelastic scattering parameters Γ_e and Γ_i can be utilized to calculate an inelastic scattering length λ_e from the probability to elastically scatter, $\Gamma_e = 1 - \exp[-t/\lambda_e]$. Solving this gives $\lambda_e = -t/(\ln(\Gamma_e) - 1)$, which is calculated for each simulation and included in the figures and is greater than the simulated thickness in all cases. Using Matthiessen's rule ($1/\lambda = 1/\lambda_e + 1/\lambda_i$) to calculate the attenuation length at 1 eV for all these samples puts them in the 10–20 nm range, which is similar to lengths measured using attenuation length studies with BEEM.^{42,44–46} This calculation and the simulations are performed using a_o and E_F for silver and are summarized in Table I. Using this methodology along with thickness dependent studies would provide a means to find these parameters for other metals and improve the accuracy of the model to capture the hot electron scattering.

TABLE I. Tabulated results from computational modeling of the BEEM threshold distributions.

	W e-beam	W Sputter	AuAg Thick	AuAg Thin	Cr p-Si	Cr n-Si
χ^2	1.79	3.66	1.56	2.53	1.30	1.24
Charge $\frac{e}{nm}$	2.59	5.18
Γ_e	22%	6%	14%	11%	6%	9%
t nm	4	3	2	4	5	2
λ_e nm	16.1	48.5	13.3	34.3	80.8	21.2
$\lambda(1 \text{ eV})$ nm	10.5	18.6	9.2	16.1	22.8	12.5

VI. CONCLUSION

A computational model that simulates Schottky barrier height distributions measured with BEEM was developed enabling extraction of the electrostatic barriers, hot electron scattering, and ionized impurity scattering that is occurring in the sample. The Cr/Si and W/Si(001) samples demonstrate the ability of the model to capture incomplete or partial silicide formation. The Au/Ag/Si samples demonstrate the ability of the model to illuminate the effects of alloying or pinch-off arising from intermixed metal species in contact with the semiconductor. These findings demonstrate the power of Schottky barrier visualization and its ability to determine the interface composition from measurements of the electrostatics with nanoscale spatial and meV energetic resolution. Inferring the interface composition from the viewpoint of the electrostatics is novel and has great potential to improve the understanding of the complex relationship between structural and electrostatic uniformity at the nanoscale.

ACKNOWLEDGMENTS

This work was supported by the National Science Foundation (DMR-1308102), the Semiconductor Research Corporation, and Center for Advanced Interconnect Science and Technology. Special thanks to Chris Stiles for helpful discussion on computational modeling.

APPENDIX A: COMPUTATIONAL MODEL ALGORITHM

The model produces a histogram of barrier heights to compare to the BEEM data based on the physics of hot-electron transport and interface electrostatics. Parameters such as the Schottky barrier height, standard deviation, elastic and inelastic scattering rates, the number of desired barriers, and position and depth of the charges at the interface are specified for each run of the model. A reproducible seed is generated from a time stamp for each simulation, which then is used to randomly populate a two-dimensional vector with a Gaussian distribution of barrier height values as specified. The size and shape of this Schottky barrier vector is made equivalent to the mapped grid of the interface that was used to acquire the BEEM spectra. Additional Schottky barrier heights are included in the vector if desired based on the

ratio. If any charges are specified this vector is modified by calculating the net Coulomb potential from the aggregate set of charges for each position in the vector.

For each location in the Schottky barrier vector the following steps are performed to determine the measured barrier height at that location:

1. The elastic scattering angle is determined from a random number.
2. An inelastic scattering probability is determined from a random number.
3. For each energy (tip bias) in the measured spectra, the inelastic scattering probability is calculated and if it occurs the electron's energy is reduced by a specified amount. Then the elastic scattering angle is applied and the energy associated with the resulting forward momentum is compared to the Schottky barrier at that location. If the barrier height is less than this "forward" energy, then the tip bias is added to the output histogram as the measured barrier height at that location.
4. A χ^2 value is computed from the model and data histograms, always keeping the best fit. The simulations end when the entire parameter space has been simulated.

Two types of random number generators are used (taus88 and random_device).⁴⁷ The former is a Tausworthe generator which uses a polynomial initialized by the time stamp generated from the reproducible seed. The latter is non-deterministic and uses implementation-defined stochastic processes to create sequences of random numbers that are uniformly distributed.

APPENDIX B: MODEL CONFIDENCE LEVELS

A rigorous approach to computational modeling involves asserting the level of confidence with each addition of parameters that changes the sum of the number of degrees of freedom associated with that model. In this work, the calculation of the degrees of freedom, $N_D = N - D$, is used to normalize χ^2 across all the models for comparison, but care must be taken to ensure that every additional parameter is meaningful. A level of confidence must be set to show that the two distributions agree without chance.

The P-values for the measured χ^2 and N_D of data and modeling presented in this paper are shown in Fig. 4 and computed utilizing

$$P - \text{value} = \int_{\chi^2}^{\infty} \frac{x^{N_D/2-1} e^{-x/2}}{2^{N_D/2} \Gamma(N_D/2)} dx, \quad (\text{B1})$$

where Γ is the gamma function.⁴⁸ A 3σ confidence level is chosen to determine valid fits to the data.

¹F. Braun, *Ann. Phys. - Leipzig* **229**, 556 (1875).

²W. Schottky, *Z. Phys.* **113**, 367 (1939).

³J. Larson and J. P. Snyder, *IEEE Trans. Electron Devices* **53**, 1048 (2006).

⁴M. Jang, Y. Kim, M. Jun, C. Choi, T. Kim, B. Park, and S. Lee, *J. Semicond. Technol. Sci.* **6**, 10 (2006).

⁵D. Connelly, C. Faulkner, D. E. Grupp, and J. S. Harris, *IEEE Trans. Nanotechnol.* **3**, 98 (2004).

⁶C. Lavoie, P. Adusumilli, A. V. Carr, J. S. J. Sweet, A. S. Ozcan, E. Levrau, N. Breil, and E. Alptekin, *ECS Trans.* **77**, 59 (2017).

⁷R. T. Tung, *Mater. Sci. Eng., R* **35**, 1 (2001).

⁸J. Tersoff, *Phys. Rev. B* **32**, 6968 (1985).

⁹R. T. Tung, *Phys. Rev. B* **45**, 13509 (1992).

¹⁰W. J. Kaiser and L. D. Bell, *Phys. Rev. Lett.* **60**, 1406 (1988).

¹¹L. D. Bell and W. J. Kaiser, *Phys. Rev. Lett.* **61**, 2368 (1988).

¹²W. Nolting, C. Durcan, A. J. Narasimham, and V. P. LaBella, *J. Vac. Sci. Technol. B* **34**, 04J110 (2016).

¹³W. Nolting, C. Durcan, and V. P. LaBella, *Appl. Phys. Lett.* **110**, 141606 (2017).

¹⁴H. Siringhaus, E. Y. Lee, and H. von Känel, *Phys. Rev. Lett.* **74**, 3999 (1995).

¹⁵C. Tivarus, J. P. Pelz, M. K. Hudait, and S. A. Ringel, *Phys. Rev. Lett.* **94**, 206803 (2005).

¹⁶L. D. Bell, *Phys. Rev. Lett.* **77**, 3893 (1996).

¹⁷R. Ludeke and M. Prietsch, *J. Vac. Sci. Technol. A* **9**, 885 (1991).

¹⁸R. Balsano, A. Matsubayashi, and V. P. LaBella, *AIP Adv.* **3**, 112110 (2013).

¹⁹M. Prietsch, *Phys. Rep.* **253**, 163 (1995).

²⁰C. P. Y. Wong, T. J. H. Koek, Y. Liu, K. P. Loh, K. E. J. Goh, C. Troadec, and C. A. Nijhuis, *ACS Appl. Mater. Interfaces* **6**, 20464 (2014).

²¹A. Junay, S. Guzo, P. Turban, G. Delhaye, B. Lpine, S. Tricot, S. Ababou-Girard, and F. Solal, *J. Appl. Phys.* **118**, 085310 (2015).

²²R. Buzio, A. Gerbia, D. Marrab, M. Barrac, and A. Cassinese, *Org. Electron.* **18**, 44 (2015).

²³A. Gerbi, R. Buzio, A. Gadaleta, L. Anghinolfi, M. Caminale, E. Bellingeri, A. S. Siri, and D. Marr, *Adv. Mater. Interfaces* **1**, 1300057 (2014).

²⁴S. Roy, C. Autieri, B. Sanyal, and T. Banerjee, *Sci. Rep.* **5**, 15747 (2015).

²⁵L. D. Bell, *J. Vac. Sci. Technol. B* **34**, 040801 (2016).

²⁶R. Holzapfel, J. Weber, P. V. Lukashev, and A. J. Stollenwerk, *J. Appl. Phys.* **123**, 174303 (2018).

²⁷H. Palm, M. Arbes, and M. Schulz, *Phys. Rev. Lett.* **71**, 2224 (1993).

²⁸H. Palm, M. Arbes, and M. Schulz, *Appl. Phys. A* **56**, 1 (1993).

²⁹K. E. J. Goh, A. Bannani, and C. Troadec, *Nanotechnology* **19**, 445718 (2008).

³⁰A. Olbrich, J. Vancea, F. Kreupl, and H. Hoffmann, *J. Appl. Phys.* **83**, 358 (1998).

³¹A. Olbrich, J. Vancea, F. Kreupl, and H. Hoffmann, *Appl. Phys. Lett.* **70**, 2559 (1997).

³²C. A. Durcan, R. Balsano, and V. P. LaBella, *J. Appl. Phys.* **116**, 023705 (2014).

³³C. A. Durcan, R. Balsano, and V. P. LaBella, *J. Appl. Phys.* **117**, 245306 (2015).

³⁴R. Balsano, C. Durcan, A. Matsubayashi, A. J. Narasimham, and V. P. LaBella, *J. Appl. Phys.* **119**, 095302 (2016).

³⁵M. Krause, A. Stollenwerk, C. Awo-Affouda, B. Maclean, and V. P. LaBella, *J. Vac. Sci. Technol. B* **23**, 1684 (2005).

³⁶E. Zarate, P. Apell, and P. M. Echenique, *Phys. Rev. B* **60**, 2326 (1999).

³⁷M. Khaidar, A. Essafti, A. Bennouna, E. L. Ameziane, and M. Brunel, *J. Appl. Phys.* **65**, 3248 (1989).

³⁸M. Aboelfotoh, *J. Appl. Phys.* **66**, 262 (1989).

³⁹Y. Jiao, A. Hellman, Y. Fang, S. Gao, and M. Kil, *Sci. Rep.* **5**, 11374 (2015).

⁴⁰T. Arizumi, M. Hirose, and N. Altaf, *Jpn. J. Appl. Phys., Part 1* **7**, 870 (1968).

⁴¹J. J. Garramone, J. R. Abel, I. L. Sitnitsky, and V. P. LaBella, *J. Vac. Sci. Technol. A* **28**, 643 (2010).

⁴²J. J. Garramone, J. R. Abel, S. Barraza-Lopez, and V. P. LaBella, *Appl. Phys. Lett.* **100**, 252102 (2012).

⁴³A. Franciosi, J. H. Weaver, and D. G. O'Neil, *Phys. Rev. B* **28**, 4889 (1983).

⁴⁴C. A. Ventrice, Jr., V. P. LaBella, G. Ramaswamy, H. P. Yu, and L. J. Schowalter, *Phys. Rev. B* **53**, 3952 (1996).

⁴⁵J. J. Garramone, J. R. Abel, I. L. Sitnitsky, L. Zhao, I. Appelbaum, and V. P. LaBella, *Appl. Phys. Lett.* **96**, 062105 (2010).

⁴⁶M. K. Weilmeyer, W. H. Rippard, and R. A. Buhrman, *Phys. Rev. B* **59**, R2521 (1999).

⁴⁷See <http://www.boost.org> for BOOST C++ Libraries.

⁴⁸W. H. Press, S. A. Teukolsky, W. T. Vetterling, and B. P. Flannery, *Numerical Recipes: The Art of Scientific Computing* (Cambridge University Press, 2007).

⁴⁹Pukelsheim, F., *American Statistician*, **48**, 88 (1994).